Received: 9 June 2024 | Revised: 19 August 2024 | Accepted: 13 September 2024

DOI: 10.1002/mrm.30324

RESEARCH ARTICLE

Magnetic Resonance in Medicine

Improved liver fat and R_2^* quantification at 0.55 T using locally low-rank denoising

Shu-Fu Shih[1,2] | **Bilal Tasdelen**[3] | **Ecrin Yagiz**[3] | **Zhaohuan Zhang**[1,2] | **Xiaodong Zhong**[1,2] | **Sophia X. Cui**[4] | **Krishna S. Nayak**[3] | **Holden H. Wu**[1,2]

[1] Department of Radiological Sciences, University of California Los Angeles, Los Angeles, California, USA

[2]Department of Bioengineering, University of California Los Angeles, Los Angeles, California, USA

[3]Ming Hsieh Department of Electrical and Computer Engineering, University of Southern California, Los Angeles, California, USA

[4]MR R&D Collaborations, Siemens Medical Solutions USA, Inc., Los Angeles, California, USA

Correspondence
Holden H. Wu, Department of Radiological Sciences, 300 UCLA Medical Plaza, Suite B119, Los Angeles, CA 90095.
Email: holdenwu@mednet.ucla.edu

Funding information
National Science Foundation, Grant/Award Number: 1828736; National Institute of Biomedical Imaging and Bioengineering, Grant/Award Number: U01EB031894; National Institute of Diabetes and Digestive and Kidney Diseases, Grant/Award Number: R01DK124417

Abstract

Purpose: To improve liver proton density fat fraction (PDFF) and R_2^* quantification at 0.55 T by systematically validating the acquisition parameter choices and investigating the performance of locally low-rank denoising methods.

Methods: A Monte Carlo simulation was conducted to design a protocol for PDFF and R_2^* mapping at 0.55 T. Using this proposed protocol, we investigated the performance of robust locally low-rank (RLLR) and random matrix theory (RMT) denoising. In a reference phantom, we assessed quantification accuracy (concordance correlation coefficient [ρ_c] vs. reference values) and precision (using SD) across scan repetitions. We performed in vivo liver scans (11 subjects) and used regions of interest to compare means and SDs of PDFF and R_2^* measurements. Kruskal–Wallis and Wilcoxon signed-rank tests were performed ($p < 0.05$ considered significant).

Results: In the phantom, RLLR and RMT denoising improved accuracy in PDFF and R_2^* with $\rho_c > 0.992$ and improved precision with >67% decrease in SD across 50 scan repetitions versus conventional reconstruction (i.e., no denoising). For in vivo liver scans, the mean PDFF and mean R_2^* were not significantly different between the three methods (conventional reconstruction; RLLR and RMT denoising). Without denoising, the SDs of PDFF and R_2^* were 8.80% and 14.17 s^{-1}. RLLR denoising significantly reduced the values to 1.79% and 5.31 s^{-1} ($p < 0.001$); RMT denoising significantly reduced the values to 2.00% and 4.81 s^{-1} ($p < 0.001$).

Conclusion: We validated an acquisition protocol for improved PDFF and R_2^* quantification at 0.55 T. Both RLLR and RMT denoising improved the accuracy and precision of PDFF and R_2^* measurements.

KEYWORDS

0.55 T MRI, denoising, liver PDFF, liver R_2^*, locally low-rank

1 | INTRODUCTION

Proton density fat fraction (PDFF)[1] and R_2^*[2] are powerful noninvasive MRI biomarkers for liver fat and iron accumulation, respectively. These two parameters can be quantified simultaneously using multi-echo gradient-echo Dixon MRI sequences followed by signal fitting to a model that resolves different confounding factors.[3–5] Several MRI sequences and signal fitting approaches have been developed and validated at 1.5 and 3 T.[3–10] Recently, MRI field strengths <1.5 T are being explored due to advantages such as reduced hardware and siting costs and reduction of artifacts in certain applications.[11–14] A lower-field MRI system with a larger bore diameter may also improve comfort[15] for populations with obesity and at risk for fatty liver disease. In addition, decreased R_2^* at lower fields can enable more accurate R_2^* quantification in patients with high iron overload.[16]

Most existing scan protocols for joint PDFF and R_2^* quantification have been designed and validated at 1.5 and/or 3 T. Adaptation to lower field strengths such as 0.55 T requires careful investigation into the trade-offs associated with acquisition parameter choices. There are several important considerations. First, lower B_0 field strengths result in lower equilibrium polarization, which reduces the SNR.[11–14] This is exacerbated when a small flip angle (FA) is used to reduce T_1-related bias in PDFF quantification.[17] Low SNR can degrade image quality and affect accuracy and precision of quantitative biomarkers.[18–20] Second, the smaller fat–water frequency difference at lower fields results in longer out-of-phase ($TE_{op} = 6.47$ ms) and in-phase ($TE_{in} = 12.94$ ms) TEs. This increases scan time and limits sequence parameter choices. Increasing the number of scan repetitions to improve SNR, a common strategy, may be infeasible in breath-holding abdominal scans. Compromises in imaging parameters such as reducing image resolution and restricting volumetric coverage can reduce diagnostic quality.

Locally low-rank principal component analysis (PCA)–based denoising is one popular approach to suppress noise in multi-contrast MR images. By suppressing principal components associated with smaller coefficients, noise can be reduced, whereas signal can be largely preserved. Difficulties in this type of method involve how to accurately estimate the signal rank and suppress the noise without removing the desired signal. Different approaches have been proposed to objectively estimate the noise level for effective noise suppression. One method, termed as *robust locally low-rank denoising* (RLLR) technique,[21] has been proposed. Using samples of random matrices from a known Gaussian distribution, the noise level in the multi-echo images can be estimated. Based on Stein's unbiased risk estimate,[22,23] the singular value threshold can be objectively obtained for noise suppression. RLLR has been shown to improve image quality for PDFF and R_2^* quantification at 3 T,[24] but it has not been studied at lower field strengths. On the other hand, *random matrix theory* (RMT)–based denoising[25–27] can accurately estimate noise level and remove the noise components by leveraging the spectral properties of random Gaussian matrices predicted by the Marchenko–Pastur Law.[28] This approach has shown promising noise suppression results, especially in diffusion MRI where many contrasts (i.e., multiple *b*-values and multiple directions) are available to construct locally low-rank patches.[25–27,29–31] There are initial studies applying RMT-based denoising for lower-field MRI,[31] but this has not yet been well studied for the application of PDFF and R_2^* mapping.

In this study, our objective is to improve liver PDFF and R_2^* quantification accuracy and precision at 0.55 T by (1) systematically refining and validating the acquisition parameter choices, and (2) investigating the performance of two locally low-rank PCA-based denoising methods: RLLR and RMT denoising. First, we performed a Monte Carlo simulation to investigate the impact of acquisition parameter choices on the accuracy and precision of PDFF and R_2^* mapping at 0.55 T. Second, we used the proposed acquisition protocol informed by simulation results and performed experiments in a reference phantom. Third, we evaluated the denoising performance in the pelvis, where high-SNR reference images can be obtained without breath-hold limitations. Fourth, we conducted experiments with breath-holding liver scans and compared the performance of PDFF and R_2^* quantification with different reconstruction/denoising algorithms.

2 | METHODS

2.1 | Acquisition protocol for PDFF and R_2^* quantification at 0.55 T

The choice of TEs and FA in the 3D multi-echo gradient-echo Dixon sequence affects PDFF and R_2^* quantification accuracy.[32–34] A common choice at 3 T is six echoes at either out-of-phase or in-phase TEs and a low FA of 3° to 5° for reducing the T_1-related bias in PDFF estimation.[5] Due to the longer out-of-phase and in-phase TEs at 0.55 T, this strategy would lead to longer TEs and TR that prolong acquisition beyond the acceptable time for one breath-hold. On the other hand, the T_1-related bias is reduced at 0.55 T because of the shortened T_1 values and the increased TR. A larger FA that balances between SNR and the T_1-related bias may be considered. Because the R_2^* values change with the field strength,[16] TEs for accurate R_2^* quantification should also be reconsidered. Therefore, we

conducted a Monte Carlo simulation to investigate different choices of FA, the first TE, and the echo spacing (ΔTE) with a range of reference PDFF and R_2^* values at 0.55 T. We limited our simulation to six echoes. This consideration was to maintain a balance between sufficient number of echoes for quantification and reasonable scan time.

The signal $s(t_m)$ at the m-th TE was simulated using the signal model:

$$s(t_m) = M\left((1-F) + F \times \left(\sum_{j=1}^{7} a_j \times e^{i2\pi f_j t_m}\right)\right) \times e^{-R_2^* t_m} \times e^{-i2\pi\varphi t_m} + n, \quad (1)$$

where M represents the steady-state magnetization signal dependent on the TE, TR, T_1, and FA; F represents the PDFF value; a_j and f_j represent the relative amplitudes and frequencies for a seven-peak fat spectrum[35]; φ represents the frequency shift due to B_0 field inhomogeneity; and n represents the complex-valued Gaussian noise.

We used T_1 of 339 and 187 ms for water and fat protons in the liver, respectively, based on previous work that measured in vivo relaxation times at 0.55 T.[36] The simulated FA were in the range of 2° to 20°. The simulated first TEs and ΔTE were both in the range of 1.2 to 2.8 ms, considering hardware specifications of the 0.55 T scanner and reasonable acquisition time of one breath-hold. The TR was set to include all the echoes and the spoiler gradient. When investigating PDFF accuracy and precision in the range of 0% to 40% (a range that covers most of the biopsy-proven metabolic dysfunction–associated steatotic liver disease patients with histologic steatosis grade 0 to 3[37]), the reference R_2^* value was fixed at 30 s^{-1} (R_2^* value at 0.55 T with no iron overload[16]). When investigating R_2^* accuracy and precision in the range of 20 to 90 s^{-1} (a range that covers mild, moderate, and no iron overload at 0.55 T[16]), the reference PDFF value was fixed at 5% (close to the common cutoff value for metabolic dysfunction–associated steatotic liver disease diagnosis[38]).

For each combination of parameters (FA, first TE, ΔTE, reference PDFF, and reference R_2^*), 500 simulated instances were generated. For each instance, φ was randomly drawn from a range of $(-100, 100)$ Hz. The complex-valued noise was modeled as $n = n_r + i \cdot n_i$, where n_r and n_i were independently drawn from a Gaussian distribution with the same variance σ^2. The value of σ^2 was set to be similar to the noise level in actual in vivo liver scans at 0.55 T. To be more specific, the resulting apparent SNR (aSNR), defined as signal mean divided by noise SD, equaled 10 when PDFF = 5%, $R_2^* = 25\ s^{-1}$, and flip angle = 8° in our Monte Carlo simulation.

All the simulated instances were fitted to a seven-peak fat model[35] with a single R_2^* decay term using a multi-step adaptive approach.[5] We measured the quantification accuracy by reporting the mean difference (MD) across instances of fitted PDFF and R_2^* versus the reference values (i.e., the bias) at different parameter settings. We measured the quantification precision by reporting the SD across instances of fitted PDFF and R_2^* at different parameter settings.

2.2 | Locally low-rank PCA-based denoising

Here, we briefly summarize the two techniques that were investigated in this work, RLLR and RMT denoising (Figure 1), and describe how we adapt them to our specific application. More technical details can be found in previous works.[21,25] In the following paragraphs, we use p_x, p_y, and p_z to represent the patch size in the three image dimensions, and use N_e and N_c to represent the number of echoes and number of coil channels, respectively.

The RLLR denoising method constructs a 2D low-rank complex valued matrix M_n with dimensions $[p_x \times p_y \times p_z$ by $N_e]$ from the coil-combined multi-echo images. Assuming the signal rank of M_n is smaller than N_e, the component associated with the smallest singular value is mainly noise. Before noise reduction, 2D random Gaussian matrix samples with dimensions $[p_x \times p_y \times p_z$ by $N_e]$ were generated using a predetermined variance σ_s^2. The median of the smallest singular values of these matrix samples, denoted as λ_m, is calculated. By comparing the smallest singular value of M_n to λ_m, the noise variance $\hat{\sigma}_n^2$ can be estimated using

$$\hat{\sigma}_n^2 = \frac{P(M_n)}{\lambda_m} \times \sigma_s^2, \quad (2)$$

while $P(\cdot)$ extracts the smallest singular values of its argument. After estimating $\hat{\sigma}_n^2$, RLLR denoising finds the optimal value for singular value soft-thresholding by minimizing Stein's unbiased risk estimate[23] and obtaining the denoised matrix. All the overlapping local patches (with stride = 1 along three spatial dimensions) are denoised using the same method and averaged to generate the final denoised images. Please note that previous works applied RLLR denoising on PDFF and R_2^* mapping at 3 T and only used a 2D low-rank matrix constructed from two image dimensions.[21,24] In this work, we extended the method to include the slice dimension.

The RMT denoising method relies on the Marchenko–Pastur law.[28] Let us consider a 2D random matrix X with dimensions [p by q] ($p \leq q$) whose entries are drawn from a Gaussian distribution of mean 0 and variance σ^2. The probability density function of the eigenvalues λ of the matrix $Y = \frac{1}{q}XX^T$ can be described by the

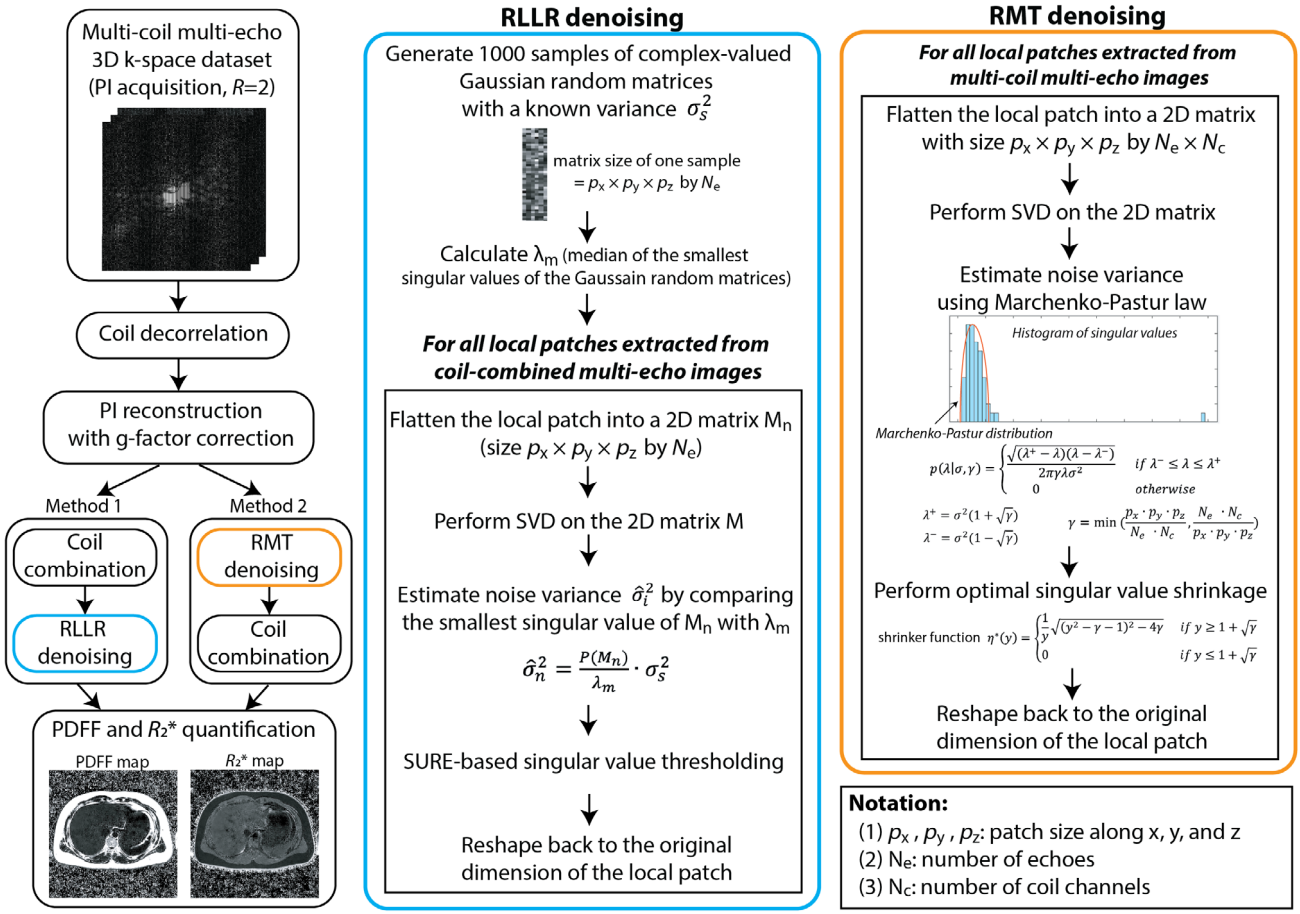

FIGURE 1 Reconstruction pipelines of the two locally low-rank principal component analysis–based denoising methods used in this work. RLLR denoising was applied on coil-combined multi-contrast images, whereas RMT denoising was applied on the multi-coil multi-contrast images. Both RLLR and RMT denoising methods needed to accurately estimate noise variance before performing singular value thresholding or shrinkage to suppress Gaussian noise. PDFF, proton density fat fraction; RLLR, robust locally low-rank; RMT, random matrix theory; SVD, singular value decomposition; SURE, Stein's unbiased risk estimate.

Marchenko–Pastur distribution:

$$p(\lambda|\sigma^2,\gamma) = \begin{cases} \frac{\sqrt{(\lambda^+-\lambda)(\lambda-\lambda^-)}}{2\pi\gamma\lambda\sigma^2} & if\ \lambda^- \le \lambda \le \lambda^+ \\ 0 & \text{otherwise} \end{cases}, \quad (3)$$

where $\lambda^+ = \sigma^2(1+\sqrt{\gamma})$, $\lambda^- = \sigma^2(1-\sqrt{\gamma})$, $\gamma = p/q$. After constructing a low-rank matrix from local image patches, noise variance σ^2 can be estimated by comparing the distribution of the singular values of the low-rank matrix to the Marchenko–Pastur distribution. Because it requires a sufficient number of eigenvalues/singular values for accurate estimation of the noise variance, we use both echo and coil dimensions to construct low-rank matrices. The real and imaginary components from the multi-coil multi-echo complex data are then concatenated to form a matrix with dimensions $[p_x \times p_y \times p_z$ by $2 \times N_e \times N_c]$. Once the noise variance is estimated, optimal singular value shrinkage based on Frobenius norm minimization[39] is used. All the overlapping local patches are denoised using the same method and averaged to generate the denoised multi-coil multi-echo images. Coil combination[40] is performed after RMT denoising.

Both denoising methods assume the noise is Gaussian-distributed. Therefore, the reconstruction pipeline includes coil decorrelation[41] and requires g-factor correction[42] for parallel imaging (PI)-accelerated data before denoising (Figure 1).

2.3 | PDFF and R_2^* phantom imaging

We validated the PDFF and R_2^* quantification accuracy using a reference phantom (Calimetrix, Madison, WI) with seven PDFF-only vials (0% to 100%, reference values provided by the vendor) and 10 R_2^*-only vials (17.7 to 1009.5 s^{-1} measured at 1.5 T, provided by the vendor). The PDFF-only vials did not have controlled R_2^* values,

and the R_2^*-only vials had no fat content. Scans were performed using a whole-body 0.55 T MRI system (prototype MAGNETOM Aera, Siemens Healthineers, Erlangen, Germany) equipped with high-performance shielded gradients (45 mT/m maximum amplitude, 200 T/m/s slew rate). Phased-array receiver coils (18-channel spine array and six-channel body array) were used, and there were $N_c = 12$ activated coil channels during the scans. To acquire phantom images with similar SNR as in the in vivo liver scans, we placed pads between phantom vials and the coils such that the space between the body array coil and the spine array coil was similar to the volume of an adult abdomen. We acquired data using a 3D multi-echo gradient-echo Dixon MRI research application sequence.[5] Key sequence parameters, based on findings from our Monte Carlo simulation, included $N_e = 6$ with TEs = (2.16, 4.32, 6.48, 8.64, 10.8, 12.96) ms, TR = 14.7 ms, FA = 8°, FOV = 300 × 300 mm^2, matrix size = 192 × 192, and slice thickness = 5 mm. PI with acceleration factor (R) of 2 was used. The scan was repeated 50 times without repositioning. Detailed sequence parameters are reported in Table 1. Each scan repetition was reconstructed individually, using three reconstruction methods: (1) conventional reconstruction with only PI reconstruction (GRAPPA) without any denoising, (2) PI reconstruction and RLLR denoising with an image patch size (p_x, p_y, p_z) = (5, 5, 5), and (3) PI reconstruction and RMT denoising with an image patch size (5, 5, 5). The reconstructed images were fitted with a multi-step adaptive approach[5] accounting for fat model complexity[35] and single R_2^* decay to generate PDFF and R_2^* maps. For a fair comparison, all the reconstruction results presented in this work were reconstructed offline with the same GRAPPA algorithm and the same fat–water-R_2^* fitting method.

The analysis consisted of two parts. First, we assessed the agreement of PDFF and R_2^* values from different reconstruction methods versus the reference for the evaluation of accuracy. In this part, results from one scan repetition were used. We placed a region of interest (ROI) in each vial and calculated the mean PDFF and R_2^*. PDFF values provided by the phantom vendor were used as the reference. To obtain the reference R_2^* values at 0.55 T, a single-slice 12-echo gradient-echo sequence was scanned and the images were fitted to a mono-exponential model.[16] Two R_2^* vials had $R_2^* > 250\ s^{-1}$ ($T_2^* < 4$ ms) at 0.55 T, which could not be reliably fitted using the specified protocol and were not included in the quantitative analysis. The phantom vials analyzed spanned the entire PDFF range (0% to 100%) and contained R_2^* values that are consistent with values reported in subjects without iron overload ($R_2^* < 45\ s^{-1}$ from previous work[16]) and with mild liver iron overload ($45\ s^{-1} < R_2^* < 91\ s^{-1}$ from previous work[16]). The MD and the concordance correlation coefficient (ρ_c)[43] between the measured PDFF and R_2^* values versus the reference were calculated to assess agreement. Linear regression was also performed. Second, we evaluated the precision by calculating the SD of quantitative measurements in each voxel across scan repetitions. The mean values of the change in PDFF and R_2^* SDs between different reconstruction methods were reported.

2.4 | In vivo pelvic imaging

Quantitatively assessing denoising performance in liver scans can be challenging due to the difficulty to obtain reference high-SNR images from multiple scan repetitions. The liver position can vary across multiple breath-holds, leading to artifacts after averaging. Therefore, we performed an experiment in the pelvis to quantify accuracy and precision of in vivo PDFF and R_2^* mapping. The experiment contained two analyses: (1) to investigate the denoising performance and the quantification accuracy under different noise levels, and (2) to investigate the quantification precision by calculating the SDs of PDFF and R_2^* measurements across scan repetitions. All in vivo experiments in this work were conducted under a Health Insurance Portability and Accountability Act–compliant study protocol approved by the institutional review board. All subjects were scanned after providing written informed consent.

For the first analysis, we scanned a healthy volunteer (29-year-old male with body-mass index [BMI] 26.4 kg/m^2) using the 3D multi-echo gradient-echo Dixon MRI research application sequence[5] with 30 scan repetitions (no repositioning). Key parameters were the same as the phantom scans except for the FOV and the in-plane resolution. We averaged the multi-coil multi-echo k-space data across the 30 repetitions to generate the "reference" k-space data. We then added complex-valued random Gaussian noise with different variances to the reference k-space data to generate synthetic pelvis datasets with different noise levels. We chose the noise variances so that the synthetic images after GRAPPA reconstruction (without any denoising) had aSNR ranging from 3 to 15 (whereas the original reference image had aSNR = 95). Here, aSNR was measured by the signal mean in a muscle ROI divided by background noise SD in coil-combined echo 3 (out-of-phase) images. We performed RLLR and RMT denoising on the synthetic images after GRAPPA reconstruction. PDFF and R_2^* maps were reconstructed using the same signal fitting method described earlier. We placed three ROIs, each with a size of 5 mm^2, in the subcutaneous fat tissue and in the muscle. Quantification accuracy was assessed by comparing mean PDFF and R_2^* in these ROIs versus the quantification results in the reference data (from 30 repetitions).

TABLE 1 Sequence parameters for phantom, in vivo pelvis, and in vivo liver MRI scans at 0.55 T.

	Phantom		In vivo pelvis	In vivo liver
	2D multi-echo gradient echo	3D multi-echo Dixon	3D multi-echo Dixon	3D multi-echo Dixon
Acquisition orientation	Axial	Axial	Axial	Axial
FOV (mm × mm)	300 × 300	300 × 300	400 × 400	380 × 380
TE (ms)	1.35, 3.5, 5.8, 8.0, 10.3, 12.6, 14.8, 17.1, 19.3, 21.6, 23.9, 26.1	2.16, 4.32, 6.48 (OP), 8.64, 10.8, 12.96 (IP)	2.16, 4.32, 6.48 (OP), 8.64, 10.8, 12.96 (IP)	2.16, 4.32, 6.48 (OP), 8.64, 10.8, 12.96 (IP)
TR (ms)	35	14.7	14.7	14.7
Matrix size	160 × 160	192 × 192	192 × 192	192 × 192
In-plane resolution (mm × mm)	1.9 × 1.9	1.6 × 1.6	2.1 × 2.1	2.0 × 2.0
Number of slices	1	8	8	8
Slice oversampling	N/A	20%	20%	20%
Slice thickness (mm)	5	5	5	5
Flip angle (°)	15	8	8	8
Bandwidth (Hz/px)	1565	590	590	590
Parallel imaging	No	GRAPPA ($R = 2$)	GRAPPA ($R = 2$)	GRAPPA ($R = 2$)
Averages	2	1	1	1
Scan time (min:s)	0:12	0:19	0:19	0:19 (breath-hold)

N/A, not applicable. OP, out of phase. IP, in phase.

For the second analysis, we scanned three healthy volunteers (3 males, age: 29.7 ± 0.6 years, BMI: 24.5 ± 2.6 kg/m^2) using the same sequence, each with 15 scan repetitions. Each repetition was reconstructed individually using three different methods: (1) conventional reconstruction without denoising, (2) RLLR denoising with a patch size (5, 5, 5), and (3) RMT denoising with a patch size (5, 5, 5). PDFF and R_2^* maps were calculated using the same signal fitting approach. To assess precision, we calculated pixel-wise SDs of PDFF and R_2^* values across 15 scan repetitions. We further calculated the percentage of voxels, which had reduced SDs of PDFF and R_2^* (meaning improved precision) in denoised results compared to conventional reconstruction results.

2.5 | In vivo liver imaging

Eleven subjects (three females and eight males, age: 39.5 ± 14.3 years, BMI: 26.3 ± 4.0 kg/m^2) were recruited and scanned. Four of the subjects (one female and three males, age: 49.5 ± 16.8 years, BMI: 29.9 ± 2.9 kg/m^2) had known fatty liver. All the subjects were scanned using the 3D multi-echo gradient-echo Dixon research application sequences[5] (Table 1) within a single breath-hold. Conventional reconstruction (no denoising, only GRAPPA) and reconstruction with the two denoising methods were performed. The same signal fitting approach was used to generate PDFF and R_2^* maps.

For each subject, three circular ROIs, each with a size of 5 mm^2, were placed on three different axial slices in the liver while avoiding large vessels.[7] Mean and SD of the PDFF and R_2^* values within each ROI were recorded. Bland–Altman analysis was performed to analyze the agreement of the quantification results between the conventional reconstruction and two different denoising methods.

We performed Kruskal–Wallis tests to investigate if there were any differences in PDFF mean, R_2^* mean, PDFF SD, and R_2^* SD in liver ROIs among the three reconstruction methods. $p < 0.05$ was considered significant. If the Kruskal–Wallis tests indicated significant differences, additional pair-wise Wilcoxon signed rank tests with Bonferroni correction for the p-values ($p < 0.05/3 = 0.017$ considered significant) were used to evaluate if there was significant difference between a pair of two reconstruction methods. For all the statistical tests, only one liver ROI measurement in the mid-slice from each subject was used.

3 | RESULTS

3.1 | Monte Carlo simulation results

The Monte Carlo simulation results from FA = 8° are in Figure 2 (complete results from different FA in Figure S1). A larger FA results in larger biases in PDFF due to T_1 differences between fat and water. In contrast, a smaller FA results in less precise PDFF and R_2^* due to lower SNR. Shorter TEs and less T_2^* weighting in the multi-echo signal also results in less precise PDFF and R_2^*. Considering the quantification accuracy and precision across a range of relevant PDFF and R_2^* values, we chose FA = 8°, first TE = 2.16 ms, and ΔTE = 2.16 ms as the preferred setting. In this design, the third TE and the sixth TE corresponded to out-of-phase and in-phase TEs at 0.55 T, respectively.

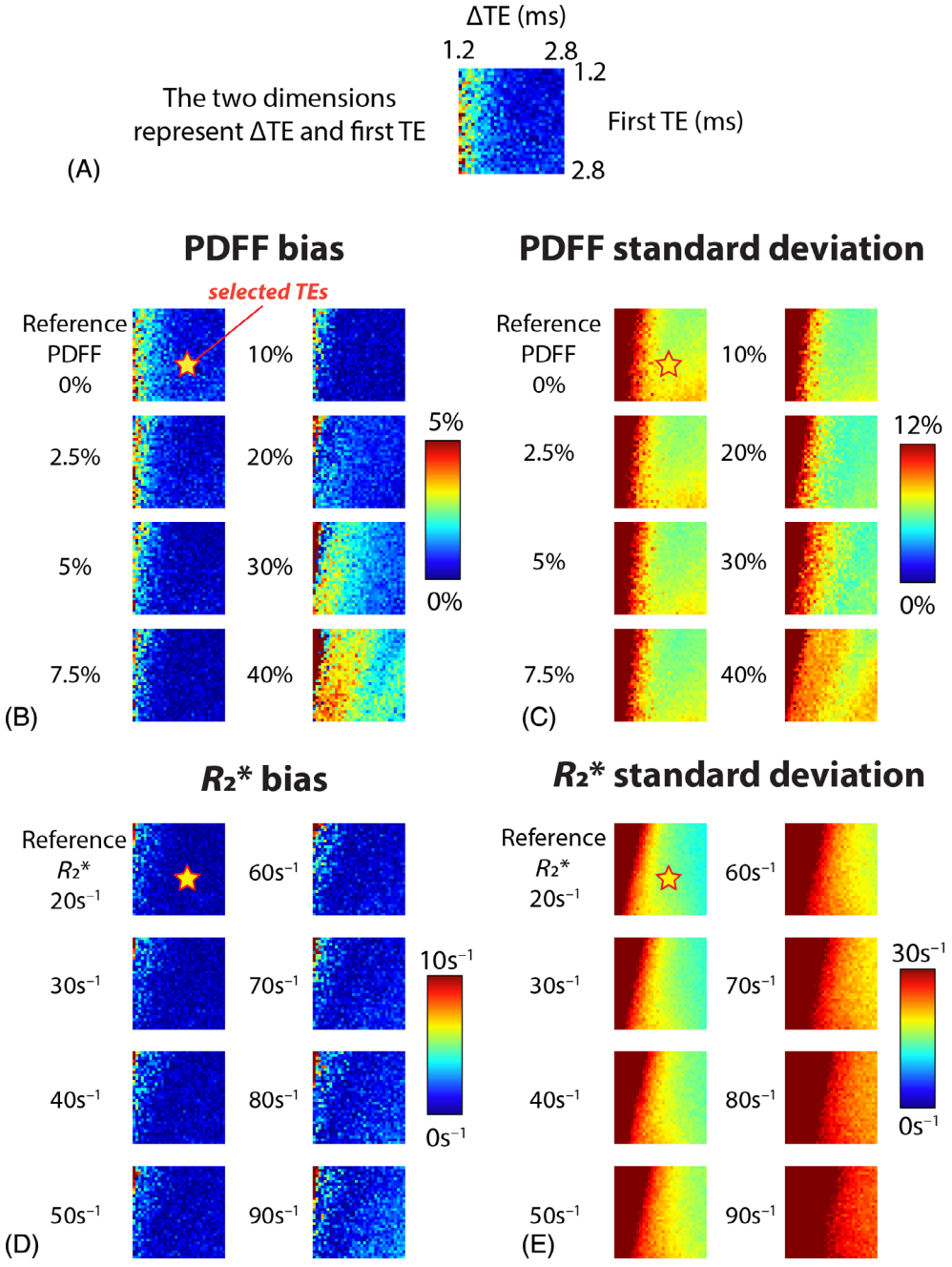

FIGURE 2 Monte Carlo simulation results of FA = 8° regarding the accuracy and precision for (A,B,C) PDFF and (D,E) R_2^* mapping using different first TE and ΔTE at 0.55 T. Complete results from different FA can be found in Figure S1. The PDFF bias and SD were reported in absolute units. To balance between accuracy and precision of parameter quantification and breath-holding scan time, we chose first TE = 2.16 ms and ΔTE = 2.16 ms as indicated by the stars. FA, flip angle.

Based on the simulation results at a representative aSNR level, our selected acquisition protocol achieved PDFF biases of 0.2% to 2% and PDFF SDs of 5.4% to 7.2% for reference PDFF values ranging from 0% to 40%. The PDFF bias and SD are reported with absolute units here and throughout this work. At the same time, our selected acquisition protocol yielded R_2^* biases of 0.2 to 2.2 s^{-1} and R_2^* SDs of 10.5 to 17.7 s^{-1} for reference R_2^* values ranging from 20 to 90 s^{-1}. Please note that these simulation results did not consider any denoising.

3.2 | PDFF and R_2^* phantom imaging results

The signal difference between denoised and non-denoised images showed minimal structured signals, demonstrating effective noise suppression without removing desired signal (Figure S2). Figure 3A,C shows quantitative maps from one scan repetition. Without denoising, large PDFF errors and noisy PDFF and R_2^* measurements were observed. Both denoising methods improved the visual quality of PDFF and R_2^* maps with reduced inhomogeneity. Figure 3B,D shows maps of pixel-wise SDs of PDFF and R_2^* values from 50 scan repetitions. Compared with conventional reconstruction, RLLR denoising showed an average of 86% and 77% decrease in PDFF and R_2^* SDs, respectively; RMT denoising showed an average of 77% and 67% decrease in PDFF and R_2^* SDs, respectively.

Compared with the reference, the MD (i.e., bias) of PDFF was 8.03% for conventional reconstruction, 0.51% for RLLR denoising, and 0.77% for RMT denoising. Compared with the reference, the MD (i.e., bias) of R_2^* was 2.08 s^{-1} for conventional reconstruction, 2.76 s^{-1} for RLLR denoising, and 3.48 s^{-1} for RMT denoising. Figure 4A,B shows the correlation plots of PDFF and R_2^* measurements between different methods and the reference. Conventional reconstruction had $\rho_c = 0.845$ in PDFF and $\rho_c = 0.984$ in R_2^* when compared with the reference. Compared with reference PDFF, RLLR denoising had $\rho_c = 0.997$ with regression result $y = 0.956x + 2.059$, and RMT denoising had $\rho_c = 0.997$ with regression result $y = 0.949x + 2.022$. Compared with reference R_2^*, RLLR denoising had $\rho_c = 0.992$ with regression result $y = 1.020x + 2.550$, and RMT denoising had $\rho_c = 0.994$ with regression result $y = 1.028x + 1.523$. Both denoising methods achieved close PDFF and R_2^* agreement with the reference.

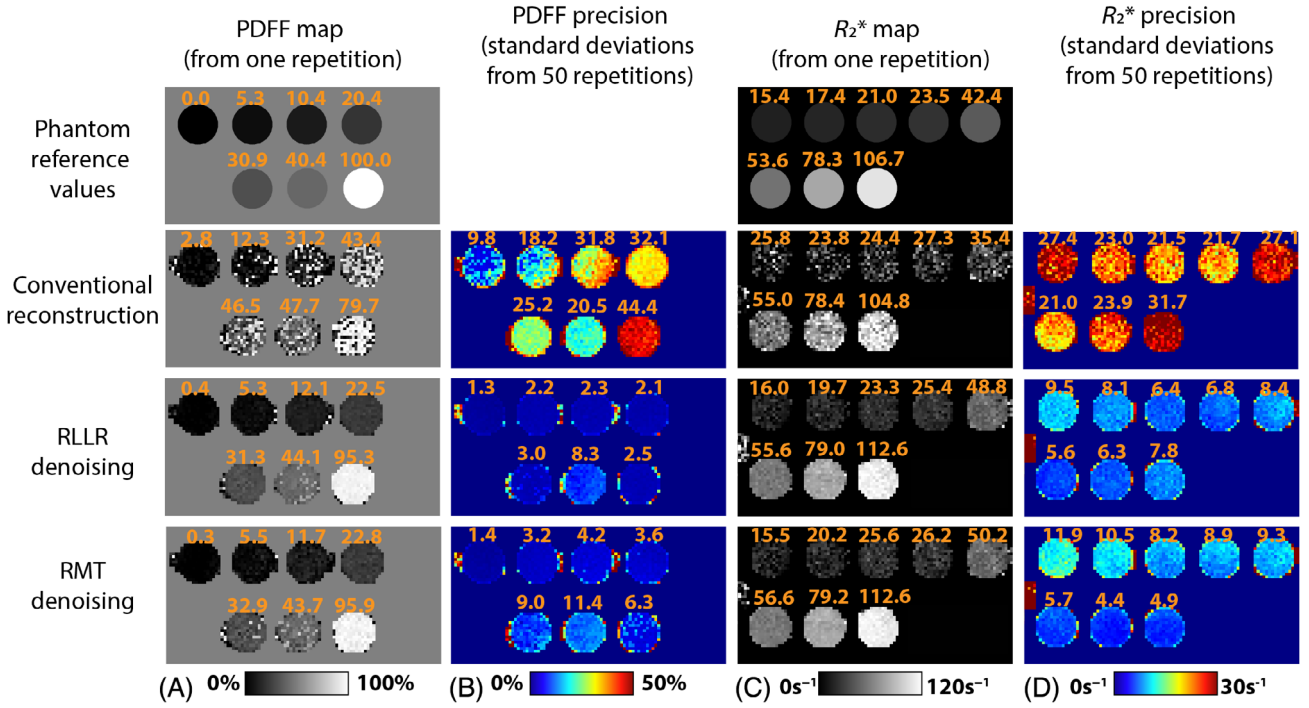

FIGURE 3 (A) PDFF quantification results in the phantom from one scan repetition. (B) Maps showing the pixelwise SD of PDFF across 50 scan repetitions. (C) R_2^* quantification results in the phantom from one scan repetition. (D) Maps showing the pixelwise SD of R_2^* across 50 scan repetitions. Numbers above each phantom vial show the measured mean value in that specific vial using a circular ROI. For example, the highest PDFF vial in the conventional reconstruction result had a mean PDFF of 79.7% and a SD of 44.4% in the circular ROI. ROI, region of interest.

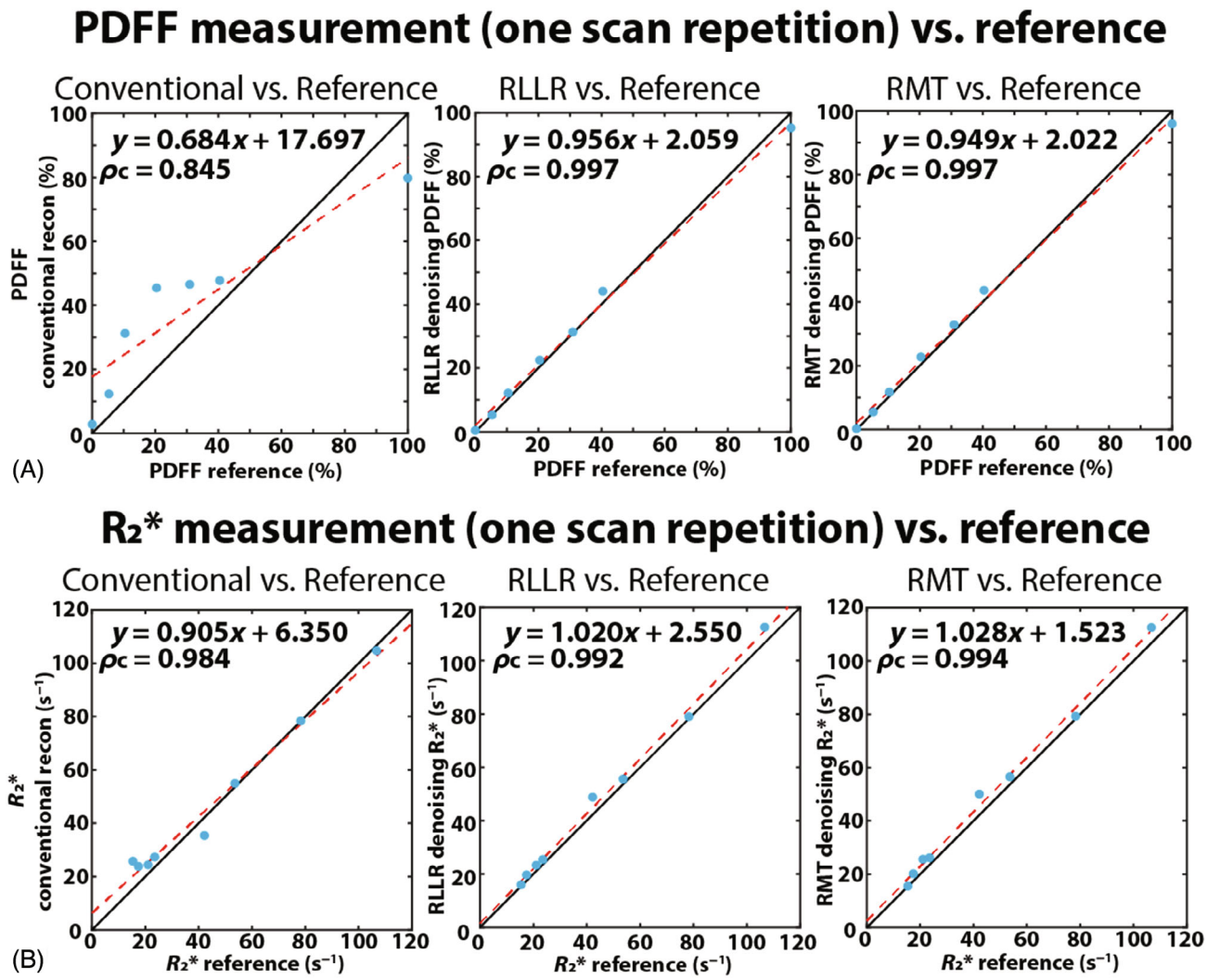

FIGURE 4 Correlation plots that compare (A) the mean PDFF measurements and (B) the mean R_2^* measurements from one scan repetition with respect to the reference values. The linear regression results and the concordance correlation coefficients (ρ_c) for each comparison are shown.

3.3 | In vivo pelvic imaging results

Figure 5A shows the reference images (aSNR = 95) and synthetic images with aSNR = 8 reconstructed with different methods. Both denoising methods reduced PDFF quantification error and provided less noisy R_2^* measurements. Without denoising, larger PDFF quantification errors were observed near the center of the body. This is consistent with the fact that the center of the body is farther away from the coil elements and the central region in the FOV has a higher g-factor and more noise amplification.

Figure 5B compares quantification results in three ROIs across different aSNR levels. Different ROIs exhibited different levels of sensitivity to aSNR. This can be due to differences in signal intensity magnitudes and the underlying PDFF and R_2^* values in different types of tissue. Both denoising methods reduced PDFF and R_2^* errors. However, for images with aSNR less than 6, a PDFF bias of 1% to 2% still existed in two ROIs after denoising.

Figure 6 shows representative pelvis MRI reconstruction results and SDs of PDFF and R_2^* measurements across 15 scan repetitions. Compared to conventional reconstruction, both denoising methods improved PDFF and R_2^* precision in terms of smaller SDs. Figure 6B,D show the scatter plots of PDFF and R_2^* SDs from one representative slice. Across all the subjects in RLLR-denoised results, the percentage of voxels with decreased PDFF and R_2^* SDs were 97.5% ± 0.3% and 98.9% ± 0.4%. Across all the subjects in RMT-denoised results, the percentage of voxels with decreased PDFF and R_2^* SDs were 96.9% ± 0.4% and 98.9% ± 0.5%.

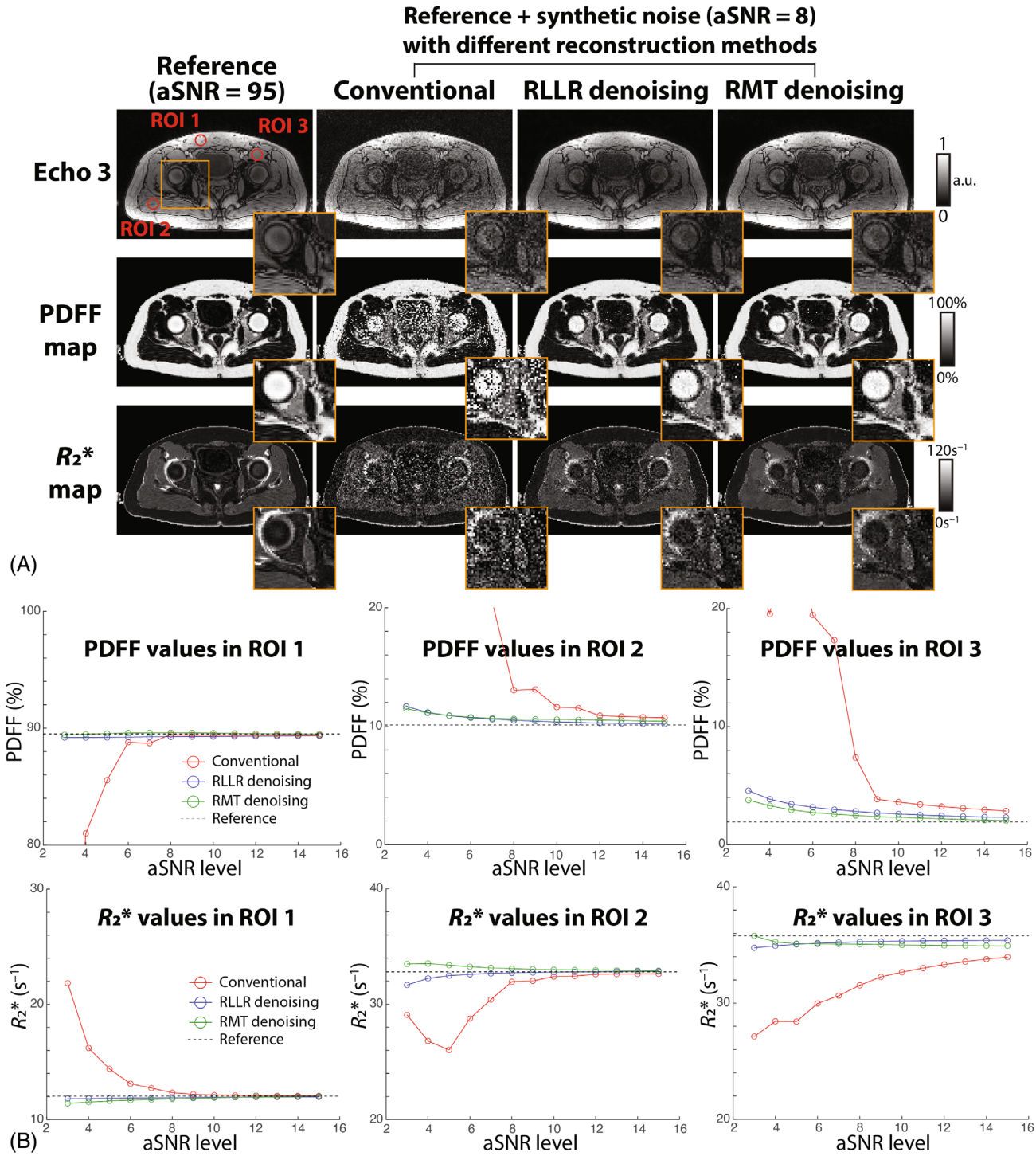

FIGURE 5 (A) Comparison of coil-combined images and quantitative maps in the synthetic pelvis dataset (aSNR = 8) reconstructed with different methods. (B) PDFF and R_2^* measurements in three ROIs (locations depicted in [A]) across different aSNR levels. Both RLLR and RMT denoising achieved better quantification accuracy (closer agreement with reference results) for PDFF and R_2^* than conventional reconstruction. aSNR, apparent SNR.

3.4 | In vivo liver imaging results

Figure 7 shows representative results from a fatty liver subject (45-year-old male, BMI = 31.6 kg/m^2). Noisy images from conventional reconstruction led to PDFF quantification error and noisy R_2^* measurements. After RLLR or RMT denoising, vessels in the liver became more discernible and the PDFF and R_2^* maps were less noisy.

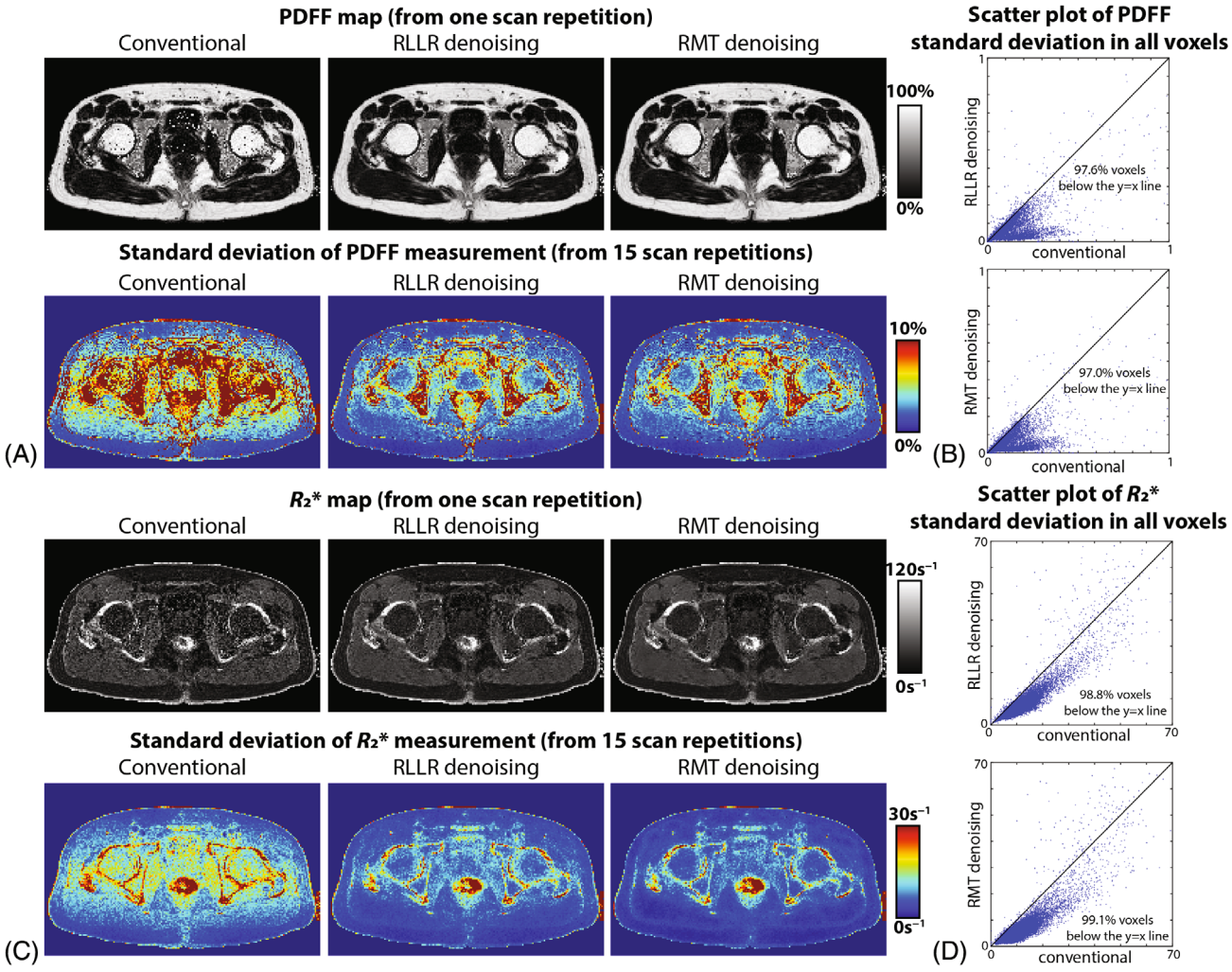

FIGURE 6 (A) Representative PDFF map and corresponding voxel-wise PDFF SD map for different methods. (B) Scatter plot of PDFF SD in all voxels (background voxels excluded). (C) Representative R_2^* map and corresponding pixel-wise R_2^* SD map for different methods. (D) Scatter plot of R_2^* SD in all voxels (background voxels excluded).

Figure 8 shows Bland–Altman plots comparing liver PDFF and R_2^* values from two denoising methods versus using conventional reconstruction. For PDFF, RLLR and RMT denoising showed a MD of −0.96% and −0.82%, respectively, when compared with conventional reconstruction. This is consistent with previous findings[44] that noise would lead to a positive PDFF bias (i.e., reducing noise can reduce the bias). On the other hand, the MD in R_2^* between denoised and non-denoised results were small, with values of 0.50 s^{-1} between RLLR denoising and conventional reconstruction and 0.55 s^{-1} between RMT denoising and conventional reconstruction.

Figure 9 shows scatter plots of PDFF and R_2^* SDs in liver ROIs from two denoising methods versus conventional reconstruction. The mean value of PDFF SDs in liver ROIs was 8.80% for conventional reconstruction and was reduced to 1.79% and 2.00% after RLLR and RMT denoising, respectively. The mean value of R_2^* SDs in liver ROIs was 14.17 s^{-1} for conventional reconstruction, and was reduced to 5.31 and 4.81 s^{-1} after RLLR and RMT denoising, respectively.

The Kruskal–Wallis ($p < 0.05$ considered significant) tests did not indicate significant differences in mean PDFF ($p = 0.209$) and mean R_2^* ($p = 0.846$) among three reconstruction methods. On the other hand, the Kruskal–Wallis tests found significant differences in PDFF SDs ($p < 0.001$) and R_2^* SDs ($p < 0.001$) among three reconstruction methods. In pair-wise Wilcoxon tests, both RLLR denoising and RMT denoising had significant differences in PDFF SDs and R_2^* SDs when compared with conventional reconstruction ($p < 0.001$ for all comparisons). There was no significant difference in PDFF SDs ($p = 0.083$) and R_2^* SDs ($p = 0.577$) between RLLR denoising and RMT denoising.

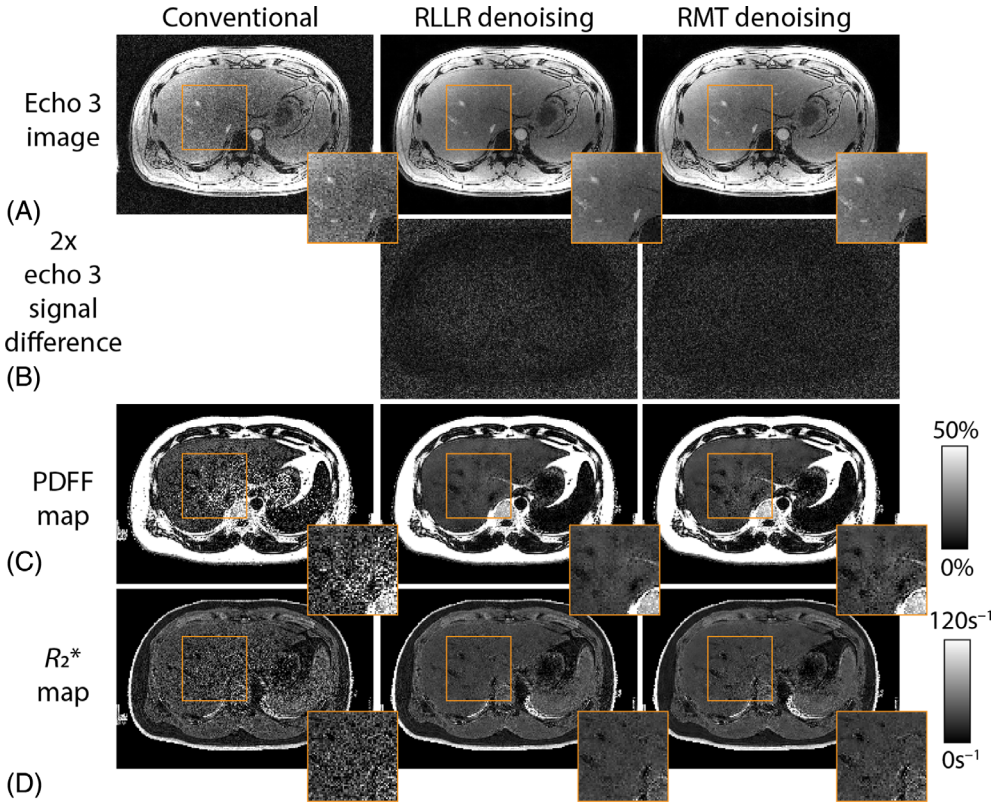

FIGURE 7 Representative result of (A) coil-combined echo 3 out-of-phase image, (B) signal difference in echo 3 image, (C) PDFF map, and (D) R_2^* map from a fatty liver subject (45-year-old male, BMI = 31.6 kg/m^2). The signal difference between conventional reconstructed and denoised images showed minimal tissue structures, demonstrating effective noise removal. Both RLLR and RMT denoising reduced PDFF quantification errors and provided less noisy R_2^* maps. BMI, body mass index.

4 | DISCUSSION

In this work, we refined and validated the acquisition parameter choices for PDFF and R_2^* quantification at 0.55 T and investigated the performance of two denoising methods to improve the quantification accuracy and precision. Based on the Monte Carlo simulation, we designed a six-echo protocol for quantifying liver PDFF and R_2^* at 0.55 T. Even with our careful design of acquisition parameters at 0.55 T, the resulting biases and appreciable SDs of PDFF and R_2^* underscored the importance and need of denoising algorithms. Using the proposed protocol in phantom and pelvis scans, we demonstrated that both RLLR and RMT denoising improved quantification accuracy in terms of close agreements with the reference and improved quantification precision in terms of reduced SDs across scan repetitions. In a cohort of 11 subjects, RLLR and RMT denoising significantly reduced SDs of PDFF and R_2^* measurements in the liver ROIs when compared to conventional reconstruction.

To determine an acquisition protocol that can estimate PDFF and R_2^* values in a range that is relevant for patient cohorts, we focused on PDFF values from 0% to 40% and R_2^* values from 20 to 90 s^{-1}. Although this range covers PDFF in fatty liver patients and mild iron overload (45 s^{-1} < R_2^* < 91 s^{-1} from previous work[16]), higher R_2^* in patients with severe iron might not be robustly estimated using the proposed protocol. Whereas longer TEs with more fat–water phase difference is beneficial for fat–water separation, quantifying higher R_2^* requires more echoes placed at shorter TEs. For these cases, the Monte Carlo simulation approach used in this work can be extended to include more relevant parameters and help design dedicated acquisition protocols.

In a previous multi-center multi-vendor PDFF phantom study,[45] the slope of the regression line is in the range of 0.86 to 1.02 at 1.5 T and 0.91 to 1.01 at 3 T using vendor protocols. The intercept of the regression line was in the range of −0.65% to 0.18% at 1.5 T and −0.78% to −0.21% at 3 T. In our phantom experiment at 0.55 T, the slopes of the regression line were 0.956 and 0.949 after RLLR and RMT denoising, demonstrating similar PDFF linearity to that at 1.5 and 3 T. The intercepts of the regression line were 2.06% and 2.02% after denoising. Even though RLLR and RMT denoising can effectively reduce the noise, a higher positive bias in PDFF is still observed at 0.55 T compared with results from 1.5 and 3 T.

From the Monte Carlo simulation and the pelvis experiment, we observed that PDFF and R_2^* accuracy can be limited when the SNR is too low. This is consistent with previous findings that noise effect can lead to PDFF bias.[18,32] It is also known that noise can bias R_2^* estimation if the signal in later echoes is close to the noise floor.[46] Whereas denoising generally improves precision without impacting accuracy, denoising may reduce quantification bias in cases when original image SNR is relatively low. In the

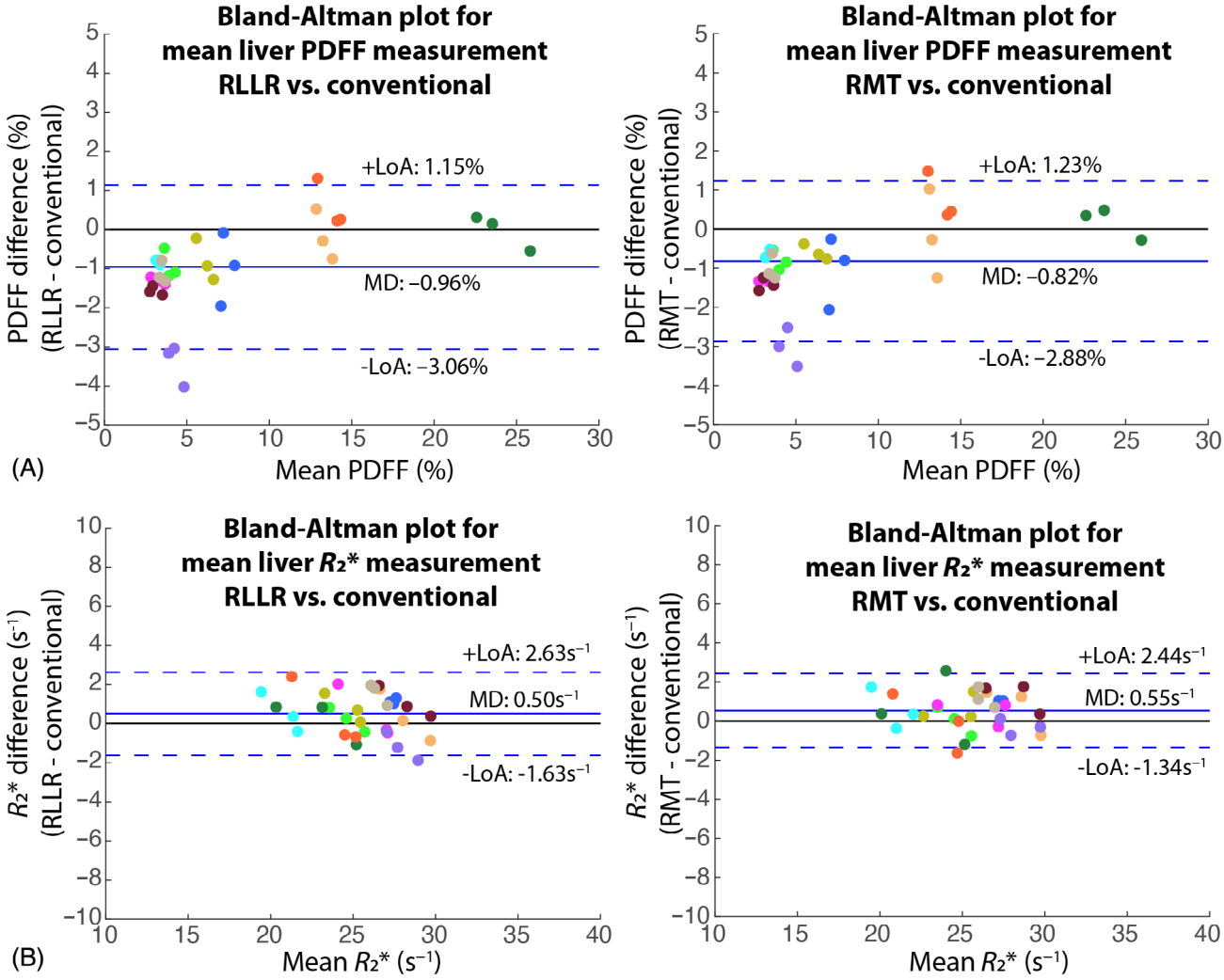

FIGURE 8 (A) Bland–Altman plots comparing mean liver PDFF measurements in results using RLLR and RMT denoising versus conventional reconstruction. (B) Bland–Altman plots comparing mean liver R_2^* measurements in results using RLLR and RMT denoising versus conventional reconstruction. Three ROIs were placed in every subject, and ROIs from the same subject were color-coded with the same color. LoA, 95% limits of agreement.

pelvis experiment, we found the denoising performance of RLLR and RMT is dependent on the original image SNR, which is affected by different factors including tissue types, acquisition parameters, proximity to the coils, and g-factor distribution if PI is used. Therefore, future improvements such as better surface coils with more elements or sampling patterns with reduced g-factor penalty are also important to further improve PDFF and R_2^* quantification at 0.55 T. We also found PDFF and R_2^* had different sensitivities to noise. Without denoising, PDFF in liver ROIs showed larger bias. On the other hand, the mean R_2^* values in liver ROIs were rather consistent with or without denoising. Nevertheless, both denoising methods can provide less noisy R_2^* maps for more precise measurements and better diagnostic quality.

The computational bottlenecks for both denoising methods were the calculations of singular value decomposition. In our 3D liver dataset, the average computational time for the denoising step (excluding PI reconstruction and signal fitting) was 1 min 10 s for RLLR denoising and 3 min 30 s for RMT denoising, using a MATLAB script with MATLAB Parallel Computing Toolbox (R2023a, MathWorks, Natick, MA) running on a 64-Core 2.7 GHz CPU (AMD Ryzen Threadripper PRO 5995WX, Santa Clara, CA). RMT denoising had longer computational time because the singular value decomposition was applied on larger 2D matrices. For both methods, computational time can be further reduced by optimizing the software implementation and running on high-performance hardware.

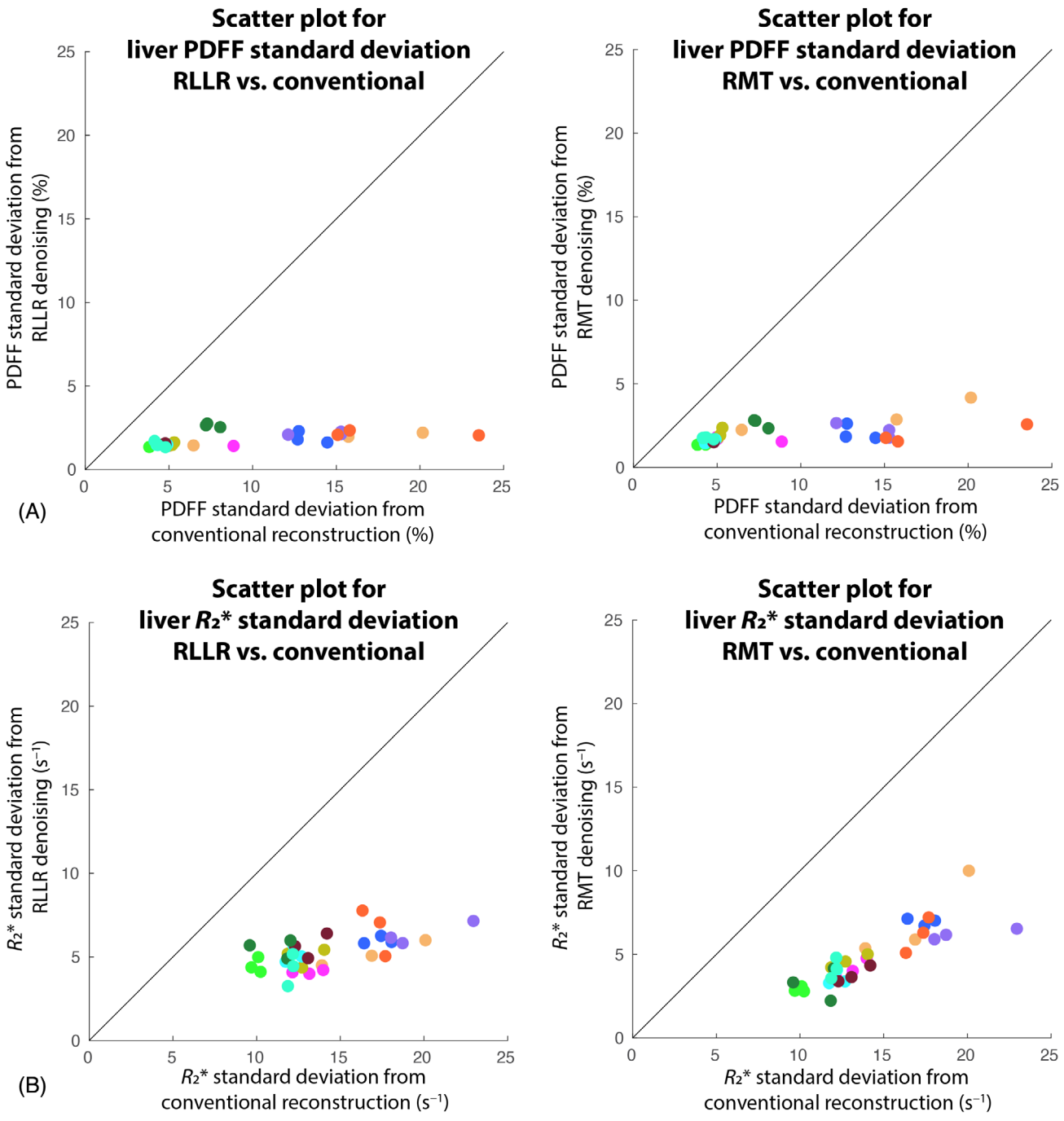

FIGURE 9 (A) Scatter plots comparing liver PDFF SD in results using RLLR and RMT denoising versus conventional reconstruction. (B) Scatter plots comparing liver R_2^* SD in results using RLLR and RMT denoising versus conventional reconstruction. Both denoising methods greatly reduced SDs of PDFF and R_2^* measurements in liver ROIs. Three ROIs were placed in every subject, and ROIs from the same subject were color-coded with the same color.

Both RLLR and RMT denoising rely on two assumptions: (1) the underlying noise is Gaussian-distributed, and (2) the low-rank property exists in local image patches. These requirements are typically met in multi-contrast MR images after noise statistics are carefully corrected. Therefore, both denoising methods can be potentially applied in many other lower-field or higher-field MRI applications in which low SNR is a problem. Even though the noise variance can be objectively estimated using these two methods, the choice of patch size is dependent on the effective signal rank and is usually based on empirical results, as used in this work and in previous locally low-rank denoising works.[21,25–27] One might need to adjust the patch size for optimal denoising performance for different datasets.

We achieved promising RMT denoising performance in our dataset by using both echo and coil dimensions to construct low-rank patches. However, this approach can be dependent on the coil configuration and should be used with caution in different datasets or scan setups. For example, if there are limited overlapping coil sensitivities in local regions, the constructed local patches may contain noise-only columns. The desired signal components therefore have a higher risk of being "drowned" in the sea of noise-related singular value components.[47] This can result in losing the desired signal components and lead to errors in final quantitative maps.

Deep learning–based methods are another promising approach for noise suppression.[48] Many deep learning–based denoising methods for lower-field MRI rely on supervised learning that requires a database of training data.[49,50] However, obtaining high-SNR reference training data from multiple scan repetitions may be difficult for abdominal scans due to breath-holding requirements. For these cases, the denoising methods investigated in this work can be used to generate training data. Another approach to improve the inherent SNR is to use non-Cartesian MRI sequences, such as radial MRI, with free-breathing acquisitions.[51–53] These techniques usually require longer scan times but can also provide robust PDFF and R_2^* quantification. Because of the higher inherent SNR, there can be more flexibility in the choice of acquisition parameters. A suitable scan protocol using non-Cartesian sequences can also be designed with the Monte Carlo simulation used in this work.

This study has limitations. First, our studied cohort had a limited size, and none of the subjects had liver iron overload ($T_2^* > 45$ ms at 0.55 T[16]). Scans in subjects with high liver iron content should be conducted in future works, and the denoising performance should be further validated. Second, our phantom analysis only included fat-only and R_2^*-only vials, which may not reflect the actual in vivo environments in the liver, where both fat and iron may be present, although this condition is rare. Further experiments should be done in phantoms with different combinations of PDFF, R_2^*, and T_1 values[54] to investigate the denoising performance and the limitations.

5 | CONCLUSION

We used a Monte Carlo simulation to design an acquisition protocol for PDFF and R_2^* quantification at 0.55 T with validation in phantom experiments. We showed that both RLLR and RMT denoising improved quantification accuracy in terms of closer agreement with the reference, and improved quantification precision in terms of reduced SDs across scan repetitions. In a cohort with healthy volunteers and fatty liver subjects, RLLR and RMT denoising both improved quantitative maps in terms of the significant decrease of PDFF and R_2^* SDs in liver ROIs when compared with conventional reconstruction.

ACKNOWLEDGMENTS

We thank Liyun Yuan for referring subjects with fatty liver and thank Mary Yung for research coordination. We thank the Dynamic Imaging Science Center (DISC) at the University of Southern California for supporting data acquisition. We thank Siemens Medical Solutions USA, Inc. for research support. The content is solely the responsibility of the authors and does not necessarily represent the official views of the National Institutes of Health.

FUNDING INFORMATION

Funding support was provided by the National Science Foundation (NSF) grant 1828736 and the National Institutes of Health (NIH) grants R01DK124417 and U01EB031894.

CONFLICT OF INTEREST STATEMENT

Coauthor Sophia X. Cui is an employee of Siemens Healthcare.

DATA AVAILABILITY STATEMENT

The MATLAB code with some example datasets is available from: https://github.com/HoldenWuLab/LLR-image-denoising

ORCID

Shu-Fu Shih https://orcid.org/0000-0002-3812-9091
Bilal Tasdelen https://orcid.org/0000-0001-6462-3651
Ecrin Yagiz https://orcid.org/0000-0001-8113-2192
Zhaohuan Zhang https://orcid.org/0000-0001-8086-6522
Xiaodong Zhong https://orcid.org/0000-0001-8355-5279
Sophia X. Cui https://orcid.org/0000-0002-5133-4903
Krishna S. Nayak https://orcid.org/0000-0001-5735-3550
Holden H. Wu https://orcid.org/0000-0002-2585-5916

TWITTER

Holden H. Wu @wuhh

REFERENCES

1. Idilman IS, Aniktar H, Idilman R, et al. Hepatic steatosis: quantification by proton density fat fraction with MR imaging versus liver biopsy. *Radiology*. 2013;267:767-775.
2. Wood JC, Enriquez C, Ghugre N, et al. MRI R2 and R2* mapping accurately estimates hepatic iron concentration in

transfusion-dependent thalassemia and sickle cell disease patients. *Blood*. 2005;106:1460-1465.
3. Hernando D, Kellman P, Haldar J, Liang ZP. Robust water/fat separation in the presence of large field inhomogeneities using a graph cut algorithm. *Magn Reson Med*. 2010;63:79-90.
4. Horng DE, Hernando D, Hines CD, Reeder SB. Comparison of R2* correction methods for accurate fat quantification in fatty liver. *J Magn Reson Imaging*. 2013;37:414-422.
5. Zhong X, Nickel MD, Kannengiesser SA, Dale BM, Kiefer B, Bashir MR. Liver fat quantification using a multi-step adaptive fitting approach with multi-echo GRE imaging. *Magn Reson Med*. 2014;72:1353-1365.
6. Artz NS, Haufe WM, Hooker CA, et al. Reproducibility of MR-based liver fat quantification across field strength: same-day comparison between 1.5 T and 3T in obese subjects. *J Magn Reson Imaging*. 2015;42:811-817.
7. Armstrong T, Zhong X, Shih S-F, et al. Free-breathing 3D stack-of-radial MRI quantification of liver fat and R2* in adults with fatty liver disease. *Magn Reson Imaging*. 2022;85:141-152.
8. Alam MH, Auger D, McGill L-A, et al. Comparison of 3 T and 1.5 T for T2* magnetic resonance of tissue iron. *J Cardiovasc Magn Reson* 2016;18:40.
9. Bashir MR, Zhong X, Nickel MD, et al. Quantification of hepatic steatosis with a multistep adaptive fitting MRI approach: prospective validation against MR spectroscopy. *Am J Roentgenol*. 2015;204:297-306.
10. Kühn J-P, Hernando D, Muñoz del Rio A, et al. Effect of multipeak spectral modeling of fat for liver iron and fat quantification: correlation of biopsy with MR imaging results. *Radiology*. 2012;265:133-142.
11. Marques JP, Simonis FF, Webb AG. Low-field MRI: an MR physics perspective. *J Magn Reson Imaging*. 2019;49:1528-1542.
12. Arnold TC, Freeman CW, Litt B, Stein JM. Low-field MRI: clinical promise and challenges. *J Magn Reson Imaging*. 2023;57:25-44.
13. Shetty AS, Ludwig DR, Ippolito JE, Andrews TJ, Narra VR, Fraum TJ. Low-field-strength body MRI: challenges and opportunities at 0.55 T. *Radiographics*. 2023;43:e230073.
14. Tian Y, Nayak KS. New clinical opportunities of low-field MRI: heart, lung, body, and musculoskeletal. *MAGMA*. 2024;37:1-14.
15. Michael AE, Heuser A, Moenninghoff C, et al. Does bore size matter?—a comparison of the subjective perception of patient comfort during low field (0.55 Tesla) and standard (1.5 Tesla). *Medicine (Baltimore)*. 2023;102:e36069.
16. Campbell-Washburn AE, Mancini C, Conrey A, et al. Evaluation of hepatic iron overload using a contemporary 0. 55 T MRI system. *J Magn Reson Imaging*. 2022;55:1855-1863.
17. Kühn JP, Jahn C, Hernando D, et al. T1 bias in chemical shift-encoded liver fat-fraction: role of the flip angle. *J Magn Reson Imaging*. 2014;40:875-883.
18. Reeder SB, Cruite I, Hamilton G, Sirlin CB. Quantitative assessment of liver fat with magnetic resonance imaging and spectroscopy. *J Magn Reson Imaging*. 2011;34:729-749.
19. Feng Y, He T, Gatehouse PD, et al. Improved MRI R2* relaxometry of iron-loaded liver with noise correction. *Magn Reson Med*. 2013;70:1765-1774.
20. Shih S-F, Cui SX, Zhong X, et al. Free-breathing liver fat quantification using radial acquisition on a high-herformance 0.55 T MRI system. *In Proceedings of the 30th Joint Annual ISMRM-ESMRMB Meeting*, London, UK; 2022:1807.
21. Lugauer F, Nickel D, Wetzl J, Kannengiesser SA, Maier A, Hornegger J. Robust spectral denoising for water-fat separation in magnetic resonance imaging. *Medical Image Computing and Computer-Assisted Intervention-MICCAI 2015: 18th International Conference, Munich, Germany, October 5–9, 2015, Proceedings, Part II 18*. Cham, Switzerland: Springer; 2015:667-674.
22. Stein CM. Estimation of the mean of a multivariate normal distribution. *Ann Statist*. 1981;9:1135-1151.
23. Candes EJ, Sing-Long CA, Trzasko JD. Unbiased risk estimates for singular value thresholding and spectral estimators. *IEEE Trans Signal Process*. 2013;61:4643-4657.
24. Allen BC, Lugauer F, Nickel D, et al. Effect of a low-rank denoising algorithm on quantitative magnetic resonance imaging-based measures of liver fat and iron. *J Comput Assist Tomogr*. 2017;41:412-416.
25. Veraart J, Novikov DS, Christiaens D, Ades-Aron B, Sijbers J, Fieremans E. Denoising of diffusion MRI using random matrix theory. *Neuroimage*. 2016;142:394-406.
26. Lemberskiy G, Baete S, Veraart J, Shepherd TM, Fieremans E, Novikov DS. Achieving sub-mm clinical diffusion MRI resolution by removing noise during reconstruction using random matrix theory. *In Proceedings of the 27th Annual Meeting of ISMRM*, Montréal, Québec, Canada; 2019:770.
27. Moeller S, Pisharady PK, Ramanna S, et al. NOise reduction with DIstribution Corrected (NORDIC) PCA in dMRI with complex-valued parameter-free locally low-rank processing. *Neuroimage*. 2021;226:117539.
28. Marchenko VA, Pastur LA. Distribution of eigenvalues for some sets of random matrices. *Matematicheskii Sbornik*. 1967;114:507-536.
29. Cordero-Grande L, Christiaens D, Hutter J, Price AN, Hajnal JV. Complex diffusion-weighted image estimation via matrix recovery under general noise models. *Neuroimage*. 2019;200:391-404.
30. Zhang Z, Aygun E, Shih S-F, Raman SS, Sung K, Wu HH. High-resolution prostate diffusion MRI using eddy current-nulled convex optimized diffusion encoding and random matrix theory-based denoising. *MAGMA*. 2024;37:603-619.
31. Lemberskiy G, Chandarana H, Bruno M, et al. Feasibility of accelerated prostate diffusion-weighted imaging on 0.55 T MRI enabled with random matrix theory denoising. *Invest Radiol*. 2023;58:720-729.
32. Liu CY, McKenzie CA, Yu H, Brittain JH, Reeder SB. Fat quantification with IDEAL gradient echo imaging: correction of bias from T1 and noise. *Magn Reson Med*. 2007;58:354-364.
33. Levin YS, Yokoo T, Wolfson T, et al. Effect of echo-sampling strategy on the accuracy of out-of-phase and in-phase multiecho gradient-echo MRI hepatic fat fraction estimation. *J Magn Reson Imaging*. 2014;39:567-575.
34. Hernando D, Kühn JP, Mensel B, et al. R2* estimation using "in-phase" echoes in the presence of fat: the effects of complex spectrum of fat. *J Magn Reson Imaging*. 2013;37:717-726.
35. Ren J, Dimitrov I, Sherry AD, Malloy CR. Composition of adipose tissue and marrow fat in humans by 1H NMR at 7 Tesla. *J Lipid Res*. 2008;49:2055-2062.
36. Campbell-Washburn AE, Ramasawmy R, Restivo MC, et al. Opportunities in interventional and diagnostic imaging by

using high-performance low-field-strength MRI. *Radiology*. 2019;293:384-393.
37. Caussy C, Reeder SB, Sirlin CB, Loomba R. Noninvasive, quantitative assessment of liver fat by MRI-PDFF as an endpoint in NASH trials. *Hepatology*. 2018;68:763-772.
38. Tang A, Tan J, Sun M, et al. Nonalcoholic fatty liver disease: MR imaging of liver proton density fat fraction to assess hepatic steatosis. *Radiology*. 2013;267:422-431.
39. Gavish M, Donoho DL. Optimal shrinkage of singular values. *IEEE Trans Inf Theory*. 2017;63:2137-2152.
40. Walsh DO, Gmitro AF, Marcellin MW. Adaptive reconstruction of phased array MR imagery. *Magn Reson Med*. 2000;43:682-690.
41. Pruessmann KP, Weiger M, Börnert P, Boesiger P. Advances in sensitivity encoding with arbitrary k-space trajectories. *Magn Reson Med*. 2001;46:638-651.
42. Breuer FA, Kannengiesser SA, Blaimer M, Seiberlich N, Jakob PM, Griswold MA. General formulation for quantitative G-factor calculation in GRAPPA reconstructions. *Magn Reson Med*. 2009;62:739-746.
43. Lawrence I, Lin K. A concordance correlation coefficient to evaluate reproducibility. *Biometrics*. 1989;45:255-268.
44. Roberts NT, Hernando D, Holmes JH, Wiens CN, Reeder SB. Noise properties of proton density fat fraction estimated using chemical shift–encoded MRI. *Magn Reson Med*. 2018;80:685-695.
45. Hu HH, Yokoo T, Bashir MR, et al. Linearity and bias of proton density fat fraction as a quantitative imaging biomarker: a multicenter, multiplatform, multivendor phantom study. *Radiology*. 2021;298:640-651.
46. Sandino CM, Kellman P, Arai AE, Hansen MS, Xue H. Myocardial T2* mapping: influence of noise on accuracy and precision. *J Cardiovasc Magn Reson*. 2015;17:7.
47. Johnstone IM, Paul D. PCA in high dimensions: an orientation. *Proc IEEE Inst Electr Electron Eng*. 2018;106:1277-1292.
48. Mazurowski MA, Buda M, Saha A, Bashir MR. Deep learning in radiology: an overview of the concepts and a survey of the state of the art with focus on MRI. *J Magn Reson Imaging*. 2019;49:939-954.
49. Koonjoo N, Zhu B, Bagnall GC, Bhutto D, Rosen M. Boosting the signal-to-noise of low-field MRI with deep learning image reconstruction. *Sci Rep*. 2021;11:8248.
50. Schmidt IL, Haag N, Shahzadi I, et al. Diagnostic image quality of a low-field (0.55 T) knee MRI protocol using deep learning image reconstruction compared with a standard (1.5 T) knee MRI protocol. *J Clin Med*. 2023;12:1916.
51. Shih S-F, Wu HH. Free-breathing MRI techniques for fat and R2* quantification in the liver. *MAGMA*. 2024;37:583-602.
52. Armstrong T, Dregely I, Stemmer A, et al. Free-breathing liver fat quantification using a multiecho 3 D stack-of-radial technique. *Magn Reson Med*. 2018;79:370-382.
53. Schneider M, Benkert T, Solomon E, et al. Free-breathing fat and R2* quantification in the liver using a stack-of-stars multi-echo acquisition with respiratory-resolved model-based reconstruction. *Magn Reson Med*. 2020;84:2592-2605.
54. Zhao R, Hamilton G, Brittain JH, Reeder SB, Hernando D. Design and evaluation of quantitative MRI phantoms to mimic the simultaneous presence of fat, iron, and fibrosis in the liver. *Magn Reson Med*. 2021;85:734-747.

SUPPORTING INFORMATION

Additional supporting information may be found in the online version of the article at the publisher's website.

Figure S1. Monte Carlo simulation results regarding the accuracy and precision for PDFF and R_2^* mapping using different flip angles (FA), first echo time (TE), and ΔTE at 0.55 T. To balance between accuracy and precision of parameter quantification and breath-holding scan time, we chose first FA = 8°, TE = 2.16 ms, and ΔTE = 2.16 ms as indicated by the stars.

Figure S2. Comparison of (a) coil-combined echo 3 (out-of-phase) and (b) coil-combined echo 6 (in-phase) images from different reconstruction methods All the images are displayed using the same window/level.

How to cite this article: Shih S-F, Tasdelen B, Yagiz E, et al. Improved liver fat and R_2 quantification at 0.55 T using locally low-rank denoising. *Magn Reson Med*. 2025;93:1348-1364. doi: 10.1002/mrm.30324